

# Effect of Severe Plastic Deformation in Machining Elucidated via Rate-Strain-Microstructure Mappings

**S. Shekhar**

Department of Materials Science  
and Engineering,  
Indian Institute of Technology—Kanpur,  
Uttar Pradesh 208016, India  
e-mail: shashank@iitk.ac.in

**S. Abolghasem**

e-mail: sea40@pitt.edu

**S. Basu**

e-mail: sab115@pitt.edu

**J. Cai**

e-mail: jic32@pitt.edu

**M. R. Shankar<sup>1</sup>**

e-mail: ravishm@pitt.edu

Department of Industrial Engineering,  
Swanson School of Engineering,  
3700 O'Hara Street,  
University of Pittsburgh,  
Pittsburgh, PA 15261

*Machining induces severe plastic deformation (SPD) in the chip and on the surface to stimulate dramatic microstructural transformations which can often result in a manufactured component with a fine-grained surface. The aim of this paper is to study the one-to-one mappings between the thermomechanics of deformation during chip formation and an array of resulting microstructural characteristics in terms of central deformation parameters—strain, strain-rate, temperature, and the corresponding Zener–Hollomon (ZH) parameter. Here, we propose a generalizable rate-strain-microstructure (RSM) framework for relating the deformation parameters to the resulting deformed grain size and interface characteristics. We utilize Oxley's model to calculate the strain and strain-rate for a given orthogonal machining condition which was also validated using digital imaging correlation-based deformation field characterization. Complementary infrared thermography in combination with a modified-Oxley's analysis was utilized to characterize the temperature in the deformation zone where the SPD at high strain-rates is imposed. These characterizations were utilized to delineate a suitable RSM phase-space composed of the strain as one axis and the ZH parameter as the other. Distinctive one-to-one mappings of various microstructures corresponding to an array of grain sizes and grain boundary distributions onto unique subspaces of this RSM space are shown. Building on the realization that the microstructure on machined surfaces is closely related to the chip microstructure derived from the primary deformation zone, this elucidation is expected to offer a reliable approach for controlling surface microstructures from orthogonal machining. [DOI: 10.1115/1.4006549]*

## 1 Introduction

It is well known that chip formation in orthogonal machining is a result of SPD involving large strains, high strain-rates that scale with the cutting speed and coupled temperature rise in the deformation zone arising from the large plastic dissipation in the deformation zone [1–5]. Such intense deformation is not only the progenitor of the chip but is also the source of SPD on the machined surface. While the microstructural consequences of such SPD on the machined surface have been recognized anecdotally [6–8], there is a lack of understanding of the interplay of how the thermomechanics of deformation during the chip formation process modify the resulting microstructure. The causes of these lacunas are even more fundamental. While it is known that SPD at large strains can lead to microstructure transformations at the nanoscale [9–11], the interactive roles of extreme strain-rates and temperatures on the nanostructural complexity is mostly unexplored in the broader areas of physical metallurgy and materials science. This lack of understanding amplifies the broader inability to map extreme strains, strain-rates, and temperatures to distinguish microstructural characteristics without which it is not possible to control and predict microstructures of surfaces created by orthogonal machining processes. Toward addressing these lacunas, a key objective of this paper is to first measure systematically, the microstructures resulting from SPD in orthogonal

machining under controlled conditions using quantitative electron microscopy. Building on these prototypical measurements, this paper then lays out a new framework for mapping microstructures resulting from SPD at extreme strains, strain-rates, and temperatures which can then offer a basis for microstructural control in orthogonal machining processes.

Microstructures from SPD in orthogonal machining are expected to emerge substantially transformed at the nanometer length-scales due to the high defect densities that are induced to accommodate the extreme deformation [12]. The property changes that accompany this nanostructural refinement can often be useful. Materials with nanostructured surface layer have also been shown to have improved mechanical and other microstructure dependent functional characteristics like corrosion, electrochemical and biological responses [13–21]. For example, it has been shown that nanostructured surface of thickness as little as 50  $\mu\text{m}$  can enhance the wear properties in Fe [21], and other studies have shown an improved fatigue life for steel with nanograined layer less than 100  $\mu\text{m}$  in thickness [19,21]. Also, nanostructured materials have been shown to exhibit novel mass transport properties like enhanced diffusion which can again be several orders of magnitude higher than that in microcrystalline materials [22,23]. Stemming from this rapid diffusion in the fine-grained state, it has been shown that improved oxidation resistance and corrosion resistance properties can result [13,14,18]. Another intriguing characteristic displayed by nanostructured surface is their biological responses, like the enhanced cell-substrate interaction for preosteoblasts on nanostructured and ultrafine grained steels [16,17]. Here, it was demonstrated that substrates with nanofine/ultrafine grains amplify cell adhesion, viability, and interconnectivity of preosteoblasts in cell cultures

<sup>1</sup>Corresponding author.

Contributed by the Manufacturing Engineering Division of ASME for publication in the JOURNAL OF MANUFACTURING SCIENCE AND ENGINEERING. Manuscript received November 29, 2010; final manuscript received March 27, 2012; published online May 7, 2012. Assoc. Editor: Burak Ozdoganlar.

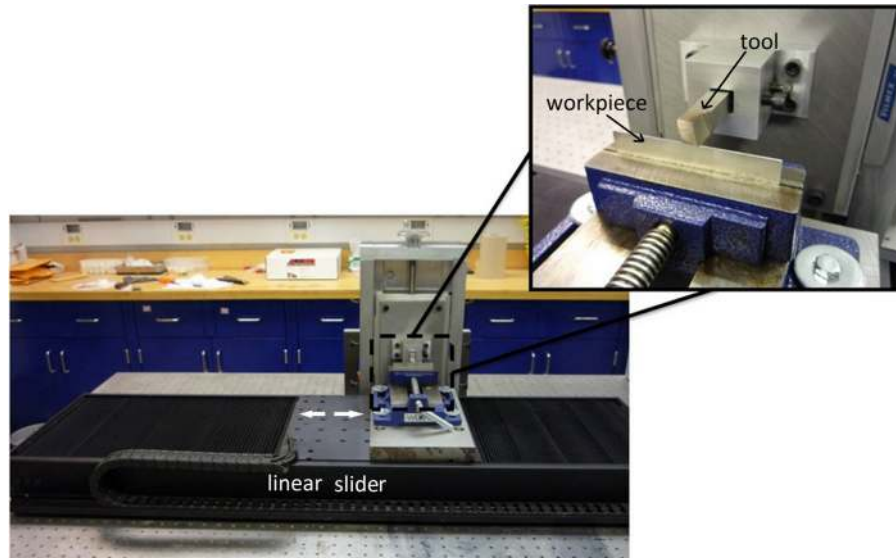


**Fig. 1 Linear test bed used for orthogonal machining**

compared to that in coarse grained materials. The discovery of such properties of nanostructured metals further motivates our pursuit of a framework for surface microstructure control during SPD in orthogonal machining which can then offer a convenient manufacturing paradigm for engineering multifunctional surface nanostructured materials.

However, reliably controlling microstructures from SPD at high strain-rates such as that in orthogonal machining is hamstrung by the lack of a broader framework that relates, one-to-one, the transformed microstructures as a function of the central deformation variables (i.e., the strain, strain-rate, and temperature). A central objective of this paper is to outline a first-of-its-kind framework for such mapping, by drawing from direct empirical and computational characterizations of a prototypical form of the metal cutting process. The overarching vision of this RSM mapping framework thus envisaged, is to offer a generalizable archetype, which can be potentially utilized for microstructure prediction in any high strain and high strain-rate process, including orthogonal machining, friction stir processing, equal channel angular pressing, high pressure torsion, etc.

## 2 Experimental Framework

Toward this objective, we first sought to undertake a rigorous electron microscopic study aimed at capturing the *quantitative* aspects of the microstructures resulting from the thermomechanics of SPD during chip formation. In this first study, we utilize commercially pure oxygen-free high thermal conductivity (OFHC) Cu as our prototypical system. Cu with its characteristic face-centered cubic (FCC) crystal structure and the lack of any phase transformations allows isolating the microstructure refinement mechanisms from other confounding effects that can occur in more complex systems. Furthermore, chip formation in Cu was found to result in typical continuous chips characterized by uniform deformation. To enable a careful elucidation of the resulting microstructure as a function of the strain, strain-rate, and temperatures of SPD, we utilize an orthogonal machining test bed (Fig. 1) that utilizes a linear electric motor to advance a plate sample past a stationary cutting tool while ensuring plane-strain conditions.

It is somewhat self-evident that the mechanics of deformation during chip formation under steady-state conditions in such a system entail uniform SPD for the chip and the surface in the direction of the cut. Of course, the freshly created surface on the workpiece would be subjected to very large strains, and the level of deformation would decline further into the bulk to ultimately converge with the characteristics of the undeformed microcrystalline material.

In earlier studies [6], it was shown through direct measurements on a similar prototypical deformation configuration how the deformation strains on the machined surface appear to converge very closely with that of the strains in the primary deformation zone. This is probably not surprising in light of the geometric contiguity of the zone that is the progenitor of both the chip and the machined surface. Furthermore, a comparison of the microstructures in the main-body of the chip with that of a zone very close to the machined surface using quantitative electron microscopy in Fig. 2 illustrates a compelling similarity between the chip and the machined surface. Figure 2 shows the microstructure taken from

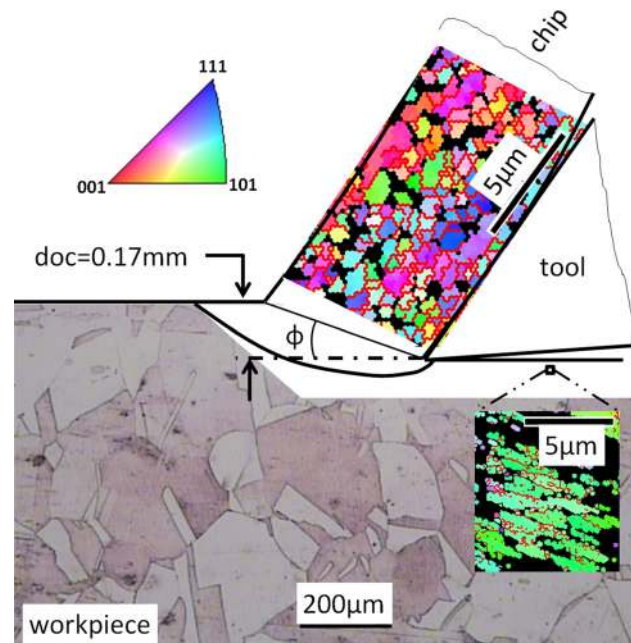


**Fig. 2 Comparison of OIM micrographs of chip (machined at 20M condition) with that near the machined surface (machined at 20M condition), where the machined surface is  $\sim 30 \mu\text{m}$  away from the top edge of the micrograph. The lines surrounding the grains in the OIM micrograph depict boundaries with grain misorientations greater than 5 deg. Optical micrograph of bulk copper showing large grains ( $\sim 200 \mu\text{m}$ ) in the undeformed region is superimposed on the workpiece region (Note: The subsurface OIM micrograph on the bottom right is approximately  $\sim 100 \mu\text{m}$  below the freshly cut surface).**

the subsurface, very close to the machined surface, and it is compared with the microstructure of the chip imaged close to its mid-point, away from its underside which would have undergone further deformation in the secondary deformation zone [24]. This illustrates the severe deformation and consequent refinement that subsurface microstructure undergoes during orthogonal machining and its unambiguous similarity to that resulting from the primary deformation zone in the machined chips.

Given this similarity that was also noted in Ref. [6], and our stated objective of quantitative microscopy of microstructural response under SPD conditions relevant to the orthogonal machining framework, it is then evident that the chip can offer a viable prototype for the intended study. From an experimental point of view, it is also known that for a first effort aimed at the quantitative analysis of nanostructures from SPD as a function of deformation conditions, it might be more viable to utilize the chips as a simpler prototype than the inhomogeneous microstructure field in the subsurface which can be unwieldy to study using electron microscopy [25]. Of course, an important caveat to consider is that this requires an examination of the chip microstructure that is directly inherited from the primary deformation zone, away from the secondary deformation zone where it accumulates further deformation that is difficult to characterize. If we can use the chip formation process as a microstructure response test for severe deformation and develop a framework for relating the thermomechanics of the deformation to the nanostructural consequences, it is then possible to utilize this knowledge-base, without loss of generality, to determine point-by-point the microstructure on the machined surface and the subsurface beneath it. While the machined surface is subjected to significant SPD, the level of this deformation declines in the subsurface with increasing distance from the deformation zone. But, the microstructural attributes of both can be effectively encapsulated if a sufficiently broad spectrum of thermomechanical conditions were examined while developing the aforementioned knowledge-base. Even otherwise, our demonstrations of the similarity of the microstructure at the machined surface and that in the chip would still ensure the utility of these results for describing the SPD nanostructures on machined surfaces.

A similar approach was adopted earlier, where the machined chips were studied as a function of machining parameters like deformation rate to describe the field of microstructures that can be obtained [20,26]. While these parameters are generally useful, they cannot be generalized for other manufacturing processes because the results relate to configuration dependent parameters such as machining speed rather than more fundamental quantities such as strain, strain-rate, and temperature. Furthermore, these earlier studies did not either utilize quantitative electron microscopy to obtain either extensive data sets on the grain sizes, or obtain detailed insights into the variation of the distribution of the misorientations between the grains which encapsulates the grain boundary structure and its energy.

Nonetheless, we build on this characterization and first identify a phase-space as a function of strain, strain-rate, and temperature which can remain universal for different processes and can be easily mapped onto other manufacturing techniques involving SPD. We further show that microstructure which is a function of three parameters (strain, strain-rate, and temperature) can actually be represented in a 2D space as a function of just two parameters, viz., strain and ZH parameter ( $Z$ ). This parameter can be calculated using [27]

$$Z = \dot{\epsilon} \exp(Q/RT) \quad (1)$$

where  $\dot{\epsilon}$  is the strain-rate,  $Q$  the activation energy for operative process,  $R$  the gas constant, and  $T$  the deformation temperature obtained earlier.

In contrast to the well established role of strain on the resulting deformed microstructures, the effect of ZH parameter which clubs together the effects from two very different parameters [27],

strain-rate and temperature is less direct. ZH parameter occurs as a critical variable in models of dislocation storage and recovery [28,29]. A big portion of the microstructure transformation during SPD in orthogonal machining occurs as a direct result of storage and rearrangement of dislocations [30,31]. It then follows that utilizing ZH may indeed offer a viable vector on a phase-space that intends to map deformation parameters to the resulting microstructures. Growing from this rationale, we will show that the 2D RSM mappings composed of ZH parameter and strain maps to regions of varying grain sizes, misorientations as well as dynamic recovery and recrystallization mechanisms. The use of ZH parameter to pin-point microstructural and constitutive response is not new. ZH parameter has been used extensively in SPD, especially in relation to Friction Stir Welding. The seminal work on this was done by Jata and Semiatin [32], and others have contributed as well [33,34]. ZH parameter has also been used in the study of recovery and recrystallization phenomenon [35,36] and it is clear from the above studies that lower ZH values and higher strain values promote recrystallization [37,38]. This is expected given that low ZH values imply higher temperature which is favorable for recrystallization.

### 3 Experimental Method

To regularize the experimental configuration for characterizing the microstructures from machining, we utilized an orthogonal machining configuration as our test bed. Here, the deformation strains ( $\epsilon$ ) are calculable for a given machining condition from the chip thickness ratio and the cutting tool rake angle using the equation [24]

$$\epsilon = \gamma/\sqrt{3} = \cos \alpha / \sqrt{3} \sin \phi \cos(\phi - \alpha) \quad (2)$$

where  $\phi$  is the shear plane angle and  $\alpha$  the rake angle. The effective strain-rate ( $\dot{\epsilon}$ ) in the deformation zone in orthogonal machining is known to scale as [7,39]

$$\dot{\epsilon} = \dot{\gamma}/\sqrt{3} = (C/\sqrt{3}) \times V_s/l \quad (3)$$

where  $V_s (= U_{work} \times \cos \alpha / \cos(\phi - \alpha))$ , the shear velocity, can be obtained directly from the knowledge of  $U_{work}$ , the deformation speed (or the cutting speed), and ' $l$ ' is the length of the deformation plane which can be obtained from depth of cut ' $d_{oc}$ ' and shear plane angle ' $\phi$ ' (see Fig. 2). In order to find the value of ' $C$ ', we utilized digital image correlation (DIC), as outlined later, to measure the values of  $\dot{\epsilon}$  using high speed images of the side-view of the deformation zone in orthogonal machining. Using these data, we calculated ' $C$ ' value for copper, whose average value was found to be 4.8 when  $V_s$  was measured in mm/s and length in millimeter.

A range of strain and strain-rate values can be realized using various rake angles and cutting speeds as expressed in the aforementioned expressions and are shown in Table 1 for the various sample conditions that were investigated for this study. As we can see from Table 1 the effective strains vary from  $\sim 2$  to 9, and effective strain-rates in the range of 50–4000/s were examined to study the resulting microstructures. It is also self-evident that the thermomechanically coupled deformation would also result in a significant variation of the temperature in the deformation zone. To identify this, we utilized a modified Oxley's model to calculate the in situ temperature rise for a given orthogonal machining condition as given in Ref. [5], to be discussed in the discussion section.

**3.1 Material System.** In this work, we used commercially pure copper bars, 2 in. in diameter, as our starting material and annealed it at 700 °C for 2 h, in order to ensure a fully coarsened starting microstructure from which to create nanostructured chips and surfaces. The average grain size after annealing was found to



**Table 1 Strain, strain-rate, temperature in the deformation zone and hardness values of various samples that were investigated (Note the hardness for bulk Cu: Hv = 46 kg f/mm<sup>2</sup>)**

Sample condition	Deformed chip thickness (mm)	$\epsilon_{EF}$ (Strain)	$\dot{\epsilon}_s$ (s <sup>-1</sup> )	$a$	$\beta$	LnZ	$T_{EF}$ (K)	Vickers hardness (kgf/mm <sup>2</sup> )
0L	2.60	8.7	60	$1.20 \times 10^{-3}$	0.95	31.11	361.4	154
0M	1.74	5.9	940	$2.10 \times 10^{-2}$	0.80	30.69	451.5	147
0H	1.45	4.9	2380	$5.46 \times 10^{-2}$	0.70	30.60	482.7	109
20L	1.77	5.9	80	$1.70 \times 10^{-3}$	0.94	32.07	344.2	163
20M	1.18	3.9	1290	$3.06 \times 10^{-2}$	0.77	32.42	409.9	161
20H	1.03	3.4	3140	$7.58 \times 10^{-2}$	0.66	32.38	436.6	159
30M	0.80	2.6	1740	$4.36 \times 10^{-2}$	0.73	33.90	377.5	154
30H	0.74	2.3	4030	$1.02 \times 10^{-1}$	0.61	33.89	400.3	152

be  $\sim 200 \mu\text{m}$ . This annealed copper rod was then machined at eight different conditions to obtain eight different sample conditions with the use of three different rake angles: 0 deg, 20 deg, and 30 deg at three different speeds: low = 50 mm/s, medium = 550 mm/s, and high = 1250 mm/s. Thus, samples from eight different orthogonal machining conditions would be referred to as 0L, 0M, 0H, 20L, 20M, 20H, 30M, and 30H, where the numbers represent the rake angle 0 deg, 20 deg, and 30 deg, respectively, and the alphabets L, M, and H refer to the three different orthogonal machining speeds, low, medium, and high, respectively. In these experiments, nominally sharp high speed steel tools that were ground into suitable geometries were utilized in the chip formation experiments.

**3.2 Mechanical Testing.** Hardness tests were conducted on all the chips obtained from different orthogonal machining conditions, using a Shimadzu microhardness tester (Vickers microhardness tester (HVM-2)). The chip samples were put in epoxy mount and polished down to  $0.05 \mu\text{m}$  using alumina suspension before being tested for hardness. A force of 490.3 mN was used for measuring the hardness values. A minimum of 10 measurements were taken to find an average value and the standard deviation. The standard deviation was found to be less than 6% for all samples.

**3.3 Orientation Indexing Microscopy (OIM).** Samples were also put in scanning electron microscope (SEM) for electron backscattered diffraction (EBSD) based OIM. This provided us with the valuable information about the microstructure like grain size, structure, crystal orientation, and the misorientation between neighboring grains. The samples for OIM were prepared by polishing with a  $0.05 \mu\text{m}$  alumina solution. OIM was carried out using Phillips XL-30 system equipped with the EDAX-Ametek EBSD detector featuring a Hikari Camera and TSL OIM software for data acquisition and analysis. All these images were taken using a step size of  $0.1 \mu\text{m}$  and the scan size was  $15 \mu\text{m} \times 15 \mu\text{m}$  for each sample except for 0H sample for which the scan size was  $25 \mu\text{m} \times 25 \mu\text{m}$ . We also used the TSL analysis software to extract information about grain size distribution, misorientation distribution, and to measure the length of regular high angle grain boundaries (HAGB) ( $>15$  deg) defined as grains for which the interfaces between the two grains (grain boundary-GB) are misoriented by  $>15$  deg and low angle grain boundaries (LAGB) (2 deg–15 deg) defined as grains for which the interfaces between the two grains are misoriented by 2–15 deg which was used in determining the fraction of LAGB for various sample conditions. We examined only the portions of the chip that were close to its midsection and away from any secondary deformation zone. This was important to ensure that we can accurately relate the microstructure consequences to the calculable thermomechanics of severe deformation in the primary deformation zone, which then offers the data required to construct the RSM framework for mapping deformation conditions to resulting nanostructural characteristics.

**3.4 Infrared (IR) Thermography.** IR thermography is a very useful tool in providing temperature near a dynamic zone

where thermocouples or other direct measurement techniques cannot be utilized. To utilize IR thermography, however, it was necessary to calibrate the system. In order to achieve this, a black stove painted calibration sample was put in front of the IR camera and radiation count values versus temperature plot was obtained by gradually increasing the temperature of the painted calibration plate. During this calibration experiment, the temperature of the plate was monitored using a thermocouple and the IR imaging was performed in the vicinity of the thermocouple. With such calibration in hand, copper workpiece was then painted using the same stove paint before orthogonal machining was performed under different conditions. IR camera was placed in front of the deformation zone while orthogonal machining, and the radiation counts were recorded and the temperature near the deformation zone was obtained using the calibrated values. A typical infrared plot obtained for a sample strained to  $\epsilon = 1.2$  at a strain-rate of  $\dot{\epsilon} = 3041 \text{ s}^{-1}$  condition is shown in Fig. 3. It is important to point out that our current thermography capabilities are limited to relatively low strain-rate conditions because of the low frame rate of the IR camera and also by its low spatial resolution where each pixel on the camera corresponds to  $\sim 20 \mu\text{m} \times 20 \mu\text{m}$  on the sample while the deformation zone itself is tens of micrometers in width.

**3.5 DIC.** The strain-rate values in the deformation zone which scale in accordance to the relationship due to Oxley and Hastings [39] was directly measured using high speed images of the deformation zone captured using a charge-coupled device (CCD) camera and the utilization of DIC, which essentially measures the Lagrangian strain by correlating image sequences of the deformation zone (see Ref. [2] for more details). We used Cooks PCO 1200hs camera which can provide us upward of 600 frames per second for this purpose. The images obtained by the camera were then analyzed using in-house developed software which can

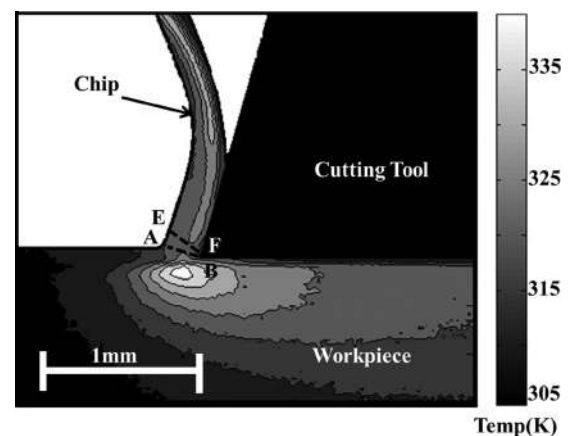


**Fig. 3 Infrared thermograph for a sample which was strained to  $\epsilon = 1.2$  at a strain-rate of  $\dot{\epsilon} = 3040 \text{ s}^{-1}$ . The calculated temperature for this orthogonal machining condition was 342 K and the measured value was 336 K.**

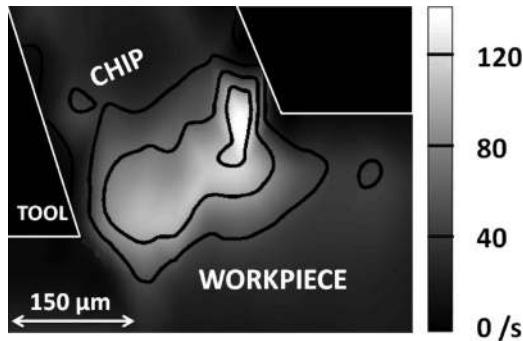


**Fig. 4 Strain-rate field obtained using DIC for copper machined using 40 deg rake angle tool at a cutting speed of 25 mm/s and doc = 0.15 mm**

recognize the asperities on the sample and use image correlation technique to identify these asperities in consecutive frames and thus measure the displacement of a given set of asperities. In order to make it easier for the software to recognize the asperities and relate it in different sets of images, the samples were loosely sprayed with black paint which not only enhanced visibility of these asperities but also formed speckle patterns which were easy to identify. These asperities and speckle patterns allowed us to create a displacement field for the deformation region and knowing the frame rate, we were eventually able to calculate strain-rate field around the deformation zone. A typical strain-rate field is shown in Fig. 4.

## 4 Results

**4.1 Hardness Values.** The hardness values of various chip samples are listed in Table 1 and the first thing that stands out is that the hardness values of all the chips are much higher compared to bulk Cu which is  $\sim 46 \text{ kg f/mm}^2$ . We also see that in general, hardness value ( $H_v$ ) for all the chip samples is approximately between 150 and 160  $\text{kg f/mm}^2$  irrespective of the strain imposed on it, which illustrates the fact that the severe deformation of the chips resulted in saturation of hardness values. However, there are two obvious anomalies to this, viz. 0H and 0M. Hardness of 0M is 147  $\text{kg f/mm}^2$  which is just a little below the range described above, however, 0H which was deformed to higher strain values than sample conditions like 20M or 20H has a hardness value of 109  $\text{kg f/mm}^2$  which is substantially below their hardness values, all of which have hardness above 150  $\text{kg f/mm}^2$ . This anomalous hardness value underscores the presence of some other factors that is influencing material properties, and one can expect a very different microstructure for this sample condition compared to the other sample conditions.

**4.2 Microstructures.** Microstructures of the chips obtained for various conditions are shown in Figs. 5(a)–5(h). We see a wide range of microstructures that can be obtained by varying the orthogonal machining parameters, and in effect, the deformation conditions like strain, strain-rate, and temperature rise in the deformation zone. The inset in Fig. 5(c) shows the triangle orientation scale of the figures. The black lines depict the grain boundaries with misorientation greater than 15 deg. The low-hardness equi-axed microstructure of 0H is conspicuous compared to the elongated grain structures of rest of the samples. Even the grain boundaries of 0H are sharply aligned—very unlike a deformed sample—while other samples have serrated grain boundaries which are a direct outcome of the severe plastic deformation that these samples were subjected to.

**4.3 Grain Size Distribution and Misorientation Distribution.** TSL software which analyzes the data obtained from OIM enabled us to obtain misorientation distribution and

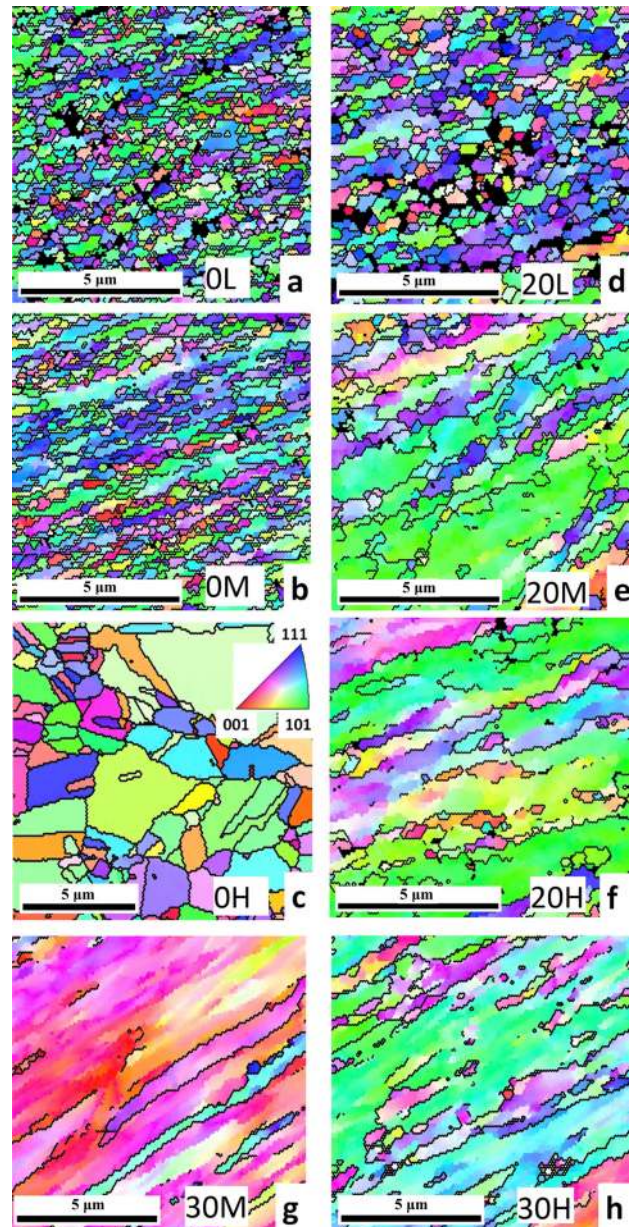


**Fig. 5 Inverse pole figure obtained using EBSD based OIM for various sample conditions: (a) 0L; (b) 0M; (c) 0H; (d) 20L; (e) 20M; (f) 20H; (g) 30M; and (h) 30H (scale markers are each 5  $\mu\text{m}$  in length). Inset in (c) displays the triangle orientation scale of the images.**

grain size distribution for various sample conditions. The misorientation plots are illustrated in Figs. 6(a)–6(h) and the grain size distributions are plotted in Figs. 7(a)–7(h). The quantitative aspects of the microstructure viz. average grain size, average HAGB misorientation, average LAGB misorientation and fraction of LAGB are summarized in Table 2.

Misorientation plots illustrate the wide variety of distributions that can be accomplished by varying the deformation conditions. 0L samples show a strongly HAGB dominated distribution while 0H shows a strongly twin-dominated distribution. 0M and 20L show a mixed distribution with almost even proportions of low angle boundaries and high angle boundaries. 20M, 20H, 30M, and 30H, on the other hand, show a very strong low angle boundary dominated distribution. 30M and 30H in particular, have negligible high angle boundaries as illustrated in the Figs. 6(g) and 6(h).



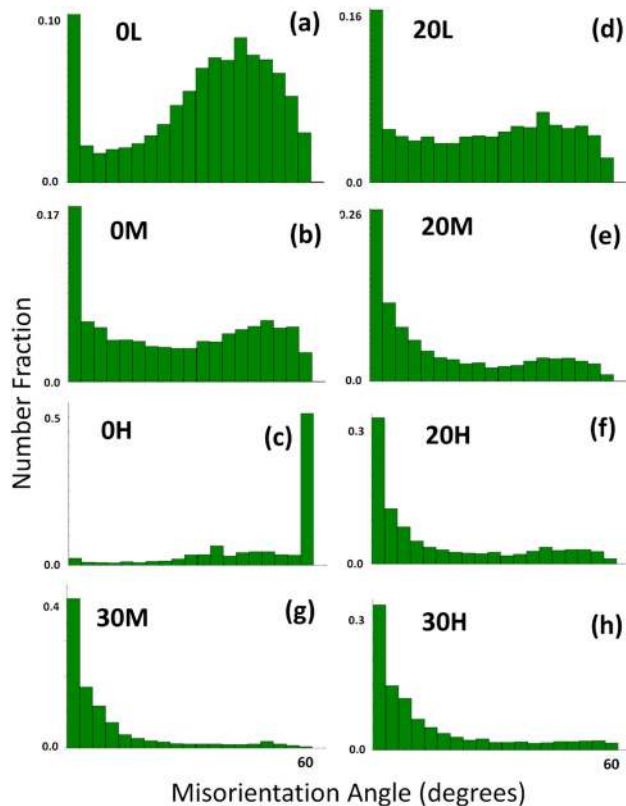


**Fig. 6** Misorientation distribution plots for various sample conditions: (a) 0L; (b) 0M; (c) 0H; (d) 20L; (e) 20M; (f) 20H; (g) 30M; and (h) 30H. 0L is strongly high angle boundary dominated. 0H is strongly twin-dominated. 0M and 20L have even distribution of low angle boundaries and high angle boundaries. 20M, 20H, 30M, and 30H are strongly low angle boundary dominated (Note: Total misorientation is 62.8 deg, hence each block represents 62.8/19 = ~3.3 deg).

The various samples studied also displayed a myriad of grain size distribution possible by merely manipulating strain and strain-rate values (Figs. 7(a)–7(h)). From the plots, we see that 0L and 20L have the smallest average grain sizes while 30M and 30H have the largest average grain sizes. All the samples, other than 0H have a significant fraction of small grains, while 0H is composed mainly of large grains, which is also evident from Fig. 5(c). Moreover, we see from the figure that some of the distributions are unimodal, while others are multimodal. The dashed-dotted lines were drawn to schematically represent the trend of the distribution. The unimodal distribution for sample conditions 0L, 0H, and 20L is obvious, while 0M is mildly multimodal. 20M, 20H, 30M, and 30H, on the other hand, are strongly multimodal. Detailed information about larger modes could not be obtained due to the small size of our scans which was limited due to the persistent problem of drift in SEM.

In Table 2, we see that average LAGB for all the sample conditions is ~7 deg while the average HAGB misorientation is ~40 deg, with the exception of 0H. The average LAGB misorientation for 0H is ~8 deg and average HAGB misorientation is 50 deg. Since the average LAGB and HAGB misorientation values are so uniform across the various sample conditions, they alone do not provide much insight into the characteristics of the microstructure. In order to extract more information from the misorientation distribution, we calculated the fraction of LAGB which was defined as the length of LAGB as fraction of total length of all grain boundaries. This value varies significantly across different sample conditions and can provide more insight about differences in various microstructures. Since, the respective averages of LAGB and HAGB are approximately same for various samples (with the exception of 0H)

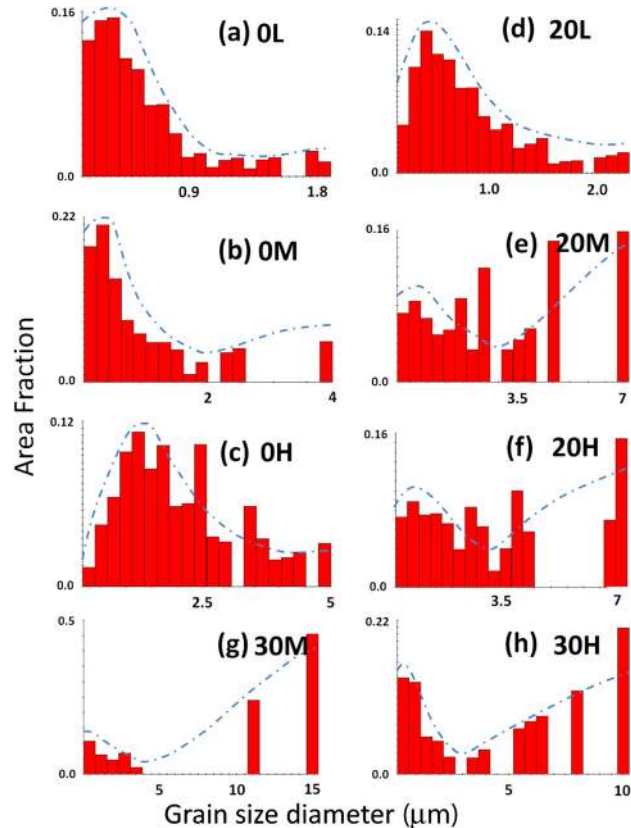


**Fig. 7** Grain size distribution plot for various sample conditions: (a) 0L; (b) 0M; (c) 0H; (d) 20L; (e) 20M; (f) 20H; (g) 30M; and (h) 30H. The dashed-dotted line show the general trend of the distribution and illustrates the unimodal distribution in 0L, 0H, and 20L, small fraction of multimodal grain distribution in 0M and strong multimodality in 20M, 20H, 30M, and 30H.

and also the shape of their distribution is similar, it also implies that the misorientation distribution of various samples can be completely characterized by single parameter: fraction of LAGBs.

## 5 Discussion

It is immediately apparent from the variety of hardness values and microstructures in Table 1 and Fig. 5 that their variation cannot be simply characterized within the conventional workhardening framework as predominantly functions of strain without taking into account the complexity that is engendered by the interactive effects of the thermomechanics of SPD. As noted earlier, SPD in orthogonal machining results in large amount of work being dissipated which predominantly gets converted into heat in the deformation zone and results in increased temperature of the workpiece and the chip. In order to calculate temperature of the deformation zone, we used Oxley's extended model, given in Ref. [5]. This modified Oxley's approach uses Johnson-Cook (JC) material model to calculate temperature in the deformation zone [40]. In this model, plane trace AB represents the region of deformation zone where the accumulated strain is approximately half that of the final strain value and plane trace EF represents the plane where full strain is expected to have been accumulated. Hence,  $\epsilon_{AB} = 1/2 \epsilon_{EF}$  and  $\epsilon_{EF}$  is the total strain in the chip. The integrated equation which was used to obtain temperature along plane EF ( $T_{EF}$ ) of Fig. 3 is given by [5]

$$\int_{T_w}^{T_{EF}} \frac{\rho C_p(T)}{1 - \left( \frac{T - T_r}{T_m - T_r} \right)^m} dT = (1 - \beta) \left( A \epsilon_{EF} + \frac{B}{n+1} \epsilon_{EF}^{n+1} \right) \times \left( 1 + C \ln \frac{\dot{\epsilon}_s}{\dot{\epsilon}_0} \right) \quad (4)$$

**Table 2 Average grain size, average misorientation and other parameters for various sample conditions (Note: Accuracy for misorientation measurement is  $\pm 0.5$  deg)**

Sample condition	Average misorientation LAGB (<15 deg)	Average misorientation HAGB (>15 deg)	Average LAGB fraction	Average grain diameter ( $\mu\text{m}$ )
0L	7.2	41.3	0.21	0.28
0M	7.4	41.0	0.36	0.35
0H	8.0	50.5	0.13	0.83
20L	7.3	40.7	0.28	0.43
20M	6.9	39.4	0.51	0.65
20H	6.8	39.1	0.58	0.74
30M	6.5	35.8	0.78	0.75
30H	7.1	37.5	0.66	0.58

where  $\rho C_p(T)$  is the heat capacity of the workpiece,  $T_w$  the temperature of the workpiece,  $T_r$  the room/reference temperature,  $T_m$  the melting temperature of the material,  $\dot{\epsilon}_0$  the reference strain-rate which is taken as  $1 \text{ s}^{-1}$ ,  $\epsilon_{\text{EF}}$  the strain at EF which is the total strain in the chip and  $\dot{\epsilon}_s$  the strain-rate in the primary shear zone which is assumed to be constant throughout the deformation zone. In above equation,  $A$ ,  $B$ ,  $C$  and  $n$  are material parameters for JC model which were obtained from Ref. [40]. Values for  $\rho C_p(T)$  which varies with temperature, were obtained by method of least square fit using cubic splines as given in Ref. [41]

$$C_p\left(\frac{T}{100}\right) = a_0 + a_1t + a_2t^2 + a_3t^3 \quad (5)$$

where  $T_{\min} \leq T \leq T_{\max}$ ,  $t = \frac{T-T_{\min}}{100}$  and the coefficients  $a_0, a_1, a_2, a_3$  vary depending on the range of  $\frac{T}{100}$ . The values for the coefficients and the input data for the fit were obtained from Ref. [41].

$T_{\text{EF}}$  is the maximum temperature to which the chip was exposed to and this is the temperature rise that results in microstructural changes in the freshly formed chip, hence, it is reasonable to compare the above temperature  $T_{\text{EF}}$  with the experimental values obtained using IR thermography.  $\beta$ , in the above equation, is the partition parameter and was obtained using model given in Ref. [42]

$$\beta = \frac{1}{4a} \text{erf} \sqrt{a} + (1+a) \text{erfc} \sqrt{a} - \frac{e^{-a}}{\sqrt{\pi}} \left( \frac{1}{2\sqrt{a}} + \sqrt{a} \right) \quad (6)$$

where ' $a$ ' is defined as  $(U_{\text{work}} \cdot d \cdot \tan \phi) / 4 \times k$ , ' $d$ ' is the feed rate (or depth of cut which for our configuration = 0.17 mm) in orthogonal machining (see Table 1 for values of  $a$  and  $\beta$ ),  $\phi$  is the primary shear plane angle,  $k$  is the thermal diffusivity of the work material ( $118 \text{ mm}^2/\text{s}$  for Cu), and  $U_{\text{work}}$  is the speed of orthogonal machining.

The calculated deformation zone temperature for various sample conditions are listed in Table 1. In order to verify the usefulness of the above model, copper samples were machined at various orthogonal machining conditions for which IR thermography was possible and their corresponding values were obtained from the analytical model described above. A comparison of some of these conditions is shown in Table 3 and it is clear from the ta-

**Table 3 Comparison of calculated temperature values ( $T_{\text{EF}}$ ) to that obtained from infrared thermography  $T_{\text{exp}}$**

Sample name	$\epsilon_{\text{EF}}$ (strain)	$\dot{\epsilon}_s$ ( $\text{s}^{-1}$ )	$T_{\text{EF}}$ (K)	$T_{\text{exp}}$ (K)
A	6.4	190	331.1	322
B	3.9	250	319.2	319
C	1.8	180	314.3	324
D	1.7	2490	359.9	378
E	1.5	330	311.2	342
F	1.3	3630	348.6	339
G	1.2	3040	342.0	336

ble that the experimentally measured values agree reasonably well with the calculated values, especially given that the temperature varies significantly in a very narrow ( $\sim$ few 10 s of  $\mu\text{m}$ ) deformation zone. It can be easily realized that the narrower the deformation zone, the greater is its measurement error. The close match between the theoretical calculations and the experimental values, underscore the validity of the thermal model used above for calculation of temperature in the deformation zone. This model was then used to calculate  $T_{\text{EF}}$  for all the sample conditions that were studied and values are provided in Table 1, and we see that temperature for these conditions varied from 360 K to 482 K.

$T_{\text{EF}}$  was also calculated for a range of conditions for copper using the above equation, and is plotted in Fig. 8 as contour maps. Here we see that temperature in the deformation zone increases with increasing strain and strain-rate, as expected. Moreover, the temperature in the deformation zone is found to be more sensitive to strain values than strain-rate which are plotted on a logarithmic scale. For all the sample conditions that were considered for this study, the deformation zone temperature is below 500 K, the highest being 483 K for 0H. This fact combined with the knowledge that 0H had the lowest hardness value, indicates that this sample condition underwent recrystallization under high stress and high strain-rate condition [43]. This is confirmed by the EBSD micrograph shown in Fig. 5(c) and by the misorientation distribution plot and grain size distribution plot. The EBSD micrograph for 0H is the only one which shows equi-axed grains with sharply defined grain boundaries. Misorientation plot for this sample condition shows that it is heavily twinned with very little fraction of LAGBs, suggesting the presence of recrystallization twins and also implying that there is negligible deformation in the sample. In the grain size distribution, the presence of very few small grains for this microstructure as compared to that of other sample

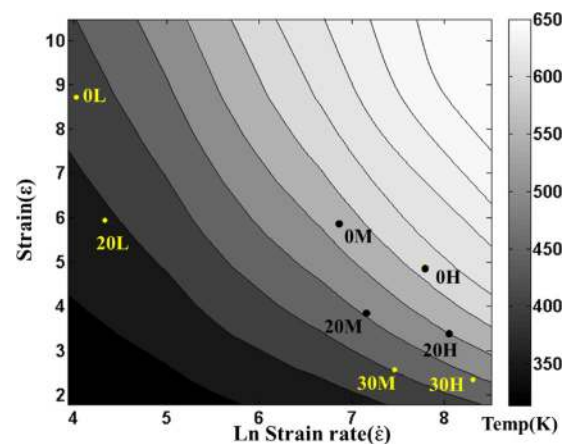


**Fig. 8 Temperature contours showing the expected temperature at plane EF of the deformation zone as a function of strain and strain-rate**

conditions is again an indication of completely recrystallized microstructure.

The sample with the next highest temperature is 0M which has a deformation zone temperature of 452 K and from the hardness value, we know that this is the softest amongst the rest of the sample conditions. However, micrographs and misorientation distribution do not suggest any kind of recrystallization taking place in this sample condition. From the small but statistically significant softening of 0M, it can be construed that recrystallization of copper chips starts at some temperature between 452 K and 483 K. Hence, coarse grained low-hardness machined surface can be obtained by utilizing orthogonal machining conditions which induces deformation zone temperature close to or higher than 483 K. If, however, fine-grained high strength material is necessitated, then it is imperative that orthogonal machining conditions should not induce temperature values higher than 452 K in the deformation zone.

The intertwined effect of temperature and strain-rate on microstructure is obvious from above results. In order to make better sense of these factors, we sought to calculate ZH parameter as this parameter merges the influence of strain-rate and temperature under one parameter. Moreover, it gives us the opportunity to present three-dimensional information on a 2D plot with the strain and the ZH parameter as the two variables encapsulating the process-space. Note that this effort envisages the use of orthogonal machining as a microstructure response test for extreme deformation for delineating a RSM framework that uniquely maps one-to-one the nanostructural characteristics to the strain and ZH (i.e., strain-rate and temperature combined together into an Arrhenius-type rate equation). Recall that once this is accomplished, it would offer a generic framework for microstructure control and design, not just on the machined surface which results from SPD under high strain-rates, but also in processes such as friction stir welding/processing, equal channel angular pressing (ECAP) and other high strain/strain-rate metal forming operations.

As noted earlier, this parameter was estimated using Eq. (1) from Ref. [27]:  $Z = \dot{\epsilon} \exp(Q/RT)$ . For  $Q$ , we utilized the grain boundary activation energy for Cu which is  $\sim 72.5 \text{ kJ mol}^{-1}$  [38], since in nanocrystalline and ultrafine-grained (UFG) materials volume density of interfaces is very high and thus even at very high temperatures it can be expected that most of the material transport will occur through grain boundary diffusion, and hence, grain boundary (GB) diffusion will be the operative mechanism for deformation processes in nanocrystalline and UFG materials. The ZH parameter was calculated for a range of strain and strain-rate conditions and a plot of  $\ln(Z)$  vs strain (note that  $\ln(Z)$  is defined as the natural logarithm of ZH parameter) which form the elements of the RSM framework is shown in Fig. 9 with the experimental sample conditions overlaid on it for a better perspective.

To make this map more useful as a predictive tool, we used statistical regression analysis to mark sections on the map that denote regions of distinct grain size distribution and misorientation distributions. 0H sample condition was intentionally left out of the regression analysis, as drastic transformations occur at 0H conditions. For strain, strain-rate condition or strain- $\ln(Z)$  conditions which result in temperature higher than that for 0H, we can expect to have a similar coarse grained recrystallized microstructure. It is below this temperature that we see interesting combination of grain size and misorientation distribution for different combinations of strain and strain-rate conditions and this is what we intend to capture using the regression analysis on the RSM maps.

Statistical regression analysis was used as a model building method to acquire an empirical relation for responses (grain size— $d$ ; LAGB fraction— $f$ ) as a function of deformation parameters, i.e., predictors, (rake angle— $\alpha$ ; orthogonal machining speed— $U_{work}$ ) using the response data obtained from quantitative electron microscopy. The statistical analysis software “Minitab” was used to obtain a simple linear regression analysis to generate grain sizes and LAGB fractions in terms of the above mentioned predictors:

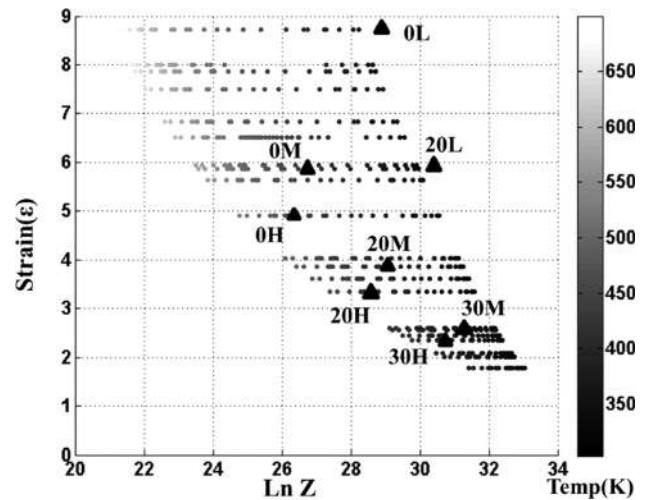


**Fig. 9** Temperature contours showing the expected temperature at plane EF of the deformation zone as a function of strain and natural logarithm of ZH parameter ( $\ln Z$ ). Experimental sample conditions are marked on the plot.

$$d = 0.292 + 0.00445 \times \alpha + 0.000323 \times U_{work}$$

and

$$f = 0.19764 + 0.00751 \times \alpha + 0.00021956 \times U_{work}$$

where  $\alpha$  is in degrees and  $U_{work}$  is in mm/s and grain size,  $d$ , is in micrometers. The above equation for grain size was used to determine the required velocity to obtain a given grain size for various rake angles. Since we possess characterizations of the strain-rate field, building on our DIC data and the strain measurements using Eq. (2), it is then possible to delineate the grain size and LAGB fractions in terms  $\ln(Z)$  and strain. This was accomplished by utilizing our data on strain and strain-rate as a function of the cutting speed that we had gathered for the various conditions, and building a second layer of regression analysis that related the deformation parameters to the strain and the strain-rate values. The deformation temperature was calculated using approaches summarized earlier. Thus, we were able to create suitable contours for equigrain size and the equi-fractions of LAGBs on the rate-strain-microstructure maps (Figs. 10 and 11, respectively).

Figure 10 demarcates the different processing conditions that can be used to obtain very fine grains or coarse grains. Fine grains can be expected to provide higher strength but lower ductility, while coarse grained microstructure can be expected to provide lower strength with higher ductility. Moreover, this map can help locate regions where significant multimodal grain size distribution can be obtained. Multimodal grain size distribution has been shown to provide high ductility along with high strength [44–47]. Furthermore, we observe that the degree of multimodality—defined as fraction of grains in larger modes—varies significantly across the sample conditions. This can be a very powerful tool in design of materials, since it is known that fraction of large grains plays a very important role in determining the mechanical properties of the materials, especially its ductility [46,48–50]. Such intricate information can be instrumental in designing a material, especially given that only surface microstructure needs to be altered to influence the overall mechanical characteristics of the material.

Figure 11 illustrates the variation of LAGB-fraction across the RSM map. As noted earlier, since the average LAGB and HAGB misorientations were very similar for all the sample conditions (other than 0H), we utilized LAGB-fraction as a parameter to describe misorientation distribution for the various sample conditions. Relative fraction of HAGBs has been shown to be related to



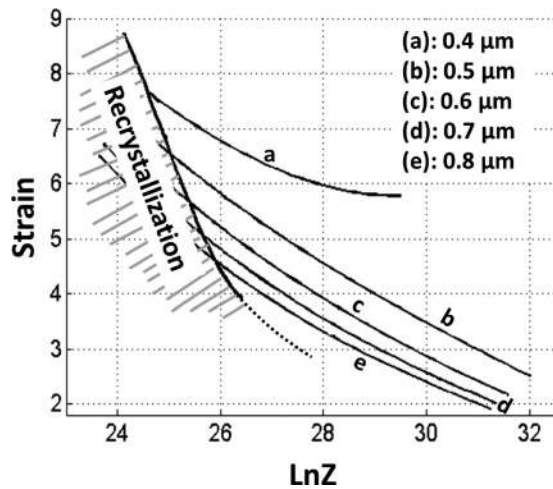


Fig. 10 Average grain size as a function of strain and Zener–Hollomon parameter. Contours show equigrainsize plots. Fine-grained microstructures are obtained toward to upper right side of the map and coarse grained microstructures are obtained toward to bottom left side of the map. Hatched region represents the condition which is expected to result in recrystallization.

the strength of the material [51]. Our recent results indicate that fraction of LAGB is related to the thermal stability of nanostructured materials (unpublished results) and further systematic studies are underway to provide concrete and conclusive evidence for the same. There are, however, other phenomena that are well known to be directly related to grain boundary characteristics, like diffusion, energy and mobility [23,52–56]. It is known that diffusivity is much faster through HAGBs and much lower through LAGBs while mobility of HAGBs is much higher than LAGBs and this difference in properties can be exploited to design components with specific application in mind. For instance, if high diffusivity is required in a material, processing conditions can be set which provide HAGB dominated microstructure, which in turn will aid high diffusivity. This can be particularly useful in manufacturing components like gears, where carbon needs to be diffused on the surface for high strength. Thus, high diffusivity would allow better penetration of carbon and hence higher strength up to greater depths of the gear tooth which can substantially increase its life and durability.

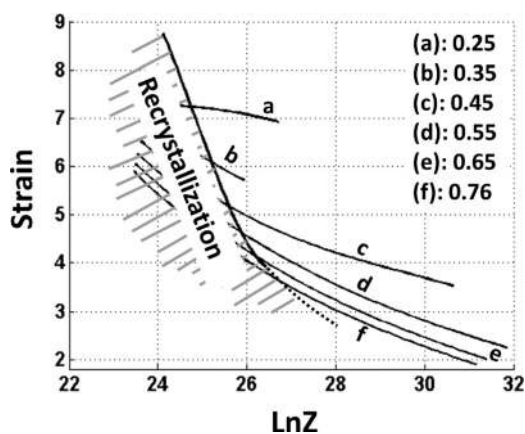


Fig. 11 LAGB as a function of strain and Zener–Hollomon parameter. Contours are equ-LAGB fraction plots. LAGB dominated microstructures are obtained toward lower-left corner of the map while HAGB dominated microstructures are obtained toward the top-right corner of the map. Hatched region represents the condition which is expected to result in recrystallization.

The results from this work is summarized in Fig. 12 which shows a “process parameter map” using the RSM framework that can be used for relating various microstructural characteristics to the processing parameters and thereby provide the ability to predict material properties. Strains below the value of 2 do not result in SPD, consequently do not produce significant changes in microstructure and hence were ignored in this map. Strain and strain-rate conditions that result in temperature as high as or higher than that for 0H can be expected to result in recrystallization and have been demarcated likewise in the map. High strain and high Ln(Z) condition can be seen to be resulting in finer grain structures while lower Ln(Z) and strain values result in coarse grain structures. This is along the expected lines since high Ln(Z) implies lower temperature and hence not enough thermal agitation for the grains to grow while lower Ln(Z), on the other hand, implies higher temperature and higher tendency for the microstructure to coarsen. Contour which was obtained from equigrainsize of  $0.4\text{ }\mu\text{m}$  is utilized as a transition between very fine grains from not so refined grains. And the contour which was obtained for  $0.7\text{ }\mu\text{m}$  grains demarcates region which produces relatively coarse grains. The region in between the two contours will have gradual change in the grain size from  $0.4\text{ }\mu\text{m}$  to  $0.7\text{ }\mu\text{m}$ .

On similar lines, high Ln(Z) and high strain conditions are expected to generate LAGB dominated microstructure, however, its variation with respect to Ln(Z) is different from that of fine-grained structure and this can lead to interesting medley of microstructures. The equ-LAGB plot with value of 0.25 and 0.45 are drawn to define LAGB dominated and HAGB dominated regions. The region above  $f=0.25$  can be interpreted as region dominated by HAGBs, while region below  $f=0.45$  can be seen as being dominated by LAGBs and in between we have mixed microstructure. The suitability of these plots to predict material properties is at once obvious when we realize that all the samples with multimodal grain size distribution lie in one corner of this plot, namely the region of intersection of high LAGBs coarse grain microstructures.

It is imperative to keep in mind that the current maps were obtained using just eight data points. However, note that the RSM maps, at this stage of its development are essentially empirically derived response maps. It is reasonable to anticipate that like any other regression-type mapping, it will capture the behavior fairly accurately in the vicinity of the data points. As more extensive data

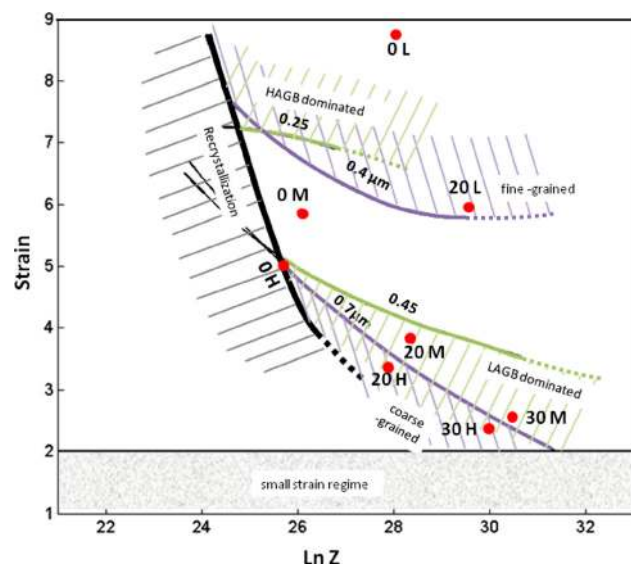


Fig. 12 RSM map for copper as a function of strain and Zener–Hollomon parameter demarcating various regions of recrystallization, HAGB dominated region, LAGB dominated region, and mixed regions. Our experimental sample conditions are also overlaid on the map.

sets become available, these mappings will become increasingly more accurate. The accuracy of the maps can be dramatically enhanced especially, when more fundamental crystal-plasticity-based models become available to accurately predict the nanostructural characteristics from SPD in machining. Taken as a whole, this map potentially offers both a process design guide to understand as well as a tool to predict the myriad of microstructures that can be obtained from SPD across a wide range of conditions.

## 6 Conclusions

Here, we present a framework for microstructure control in SPD by orthogonal machining that maps resulting nanostructural characteristics such as grain size distribution and misorientation distribution to unique regions of a suitably defined phase-space. A strain- $\ln(Z)$  space is proposed as a candidate space for developing these interconnections to ultimately encapsulate the relationships within a Rate-Strain-Microstructure map. The map captures the relevant process-microstructure relationships under strain, strain-rate, and temperature conditions that are relevant to the orthogonal machining process. Particular focus is devoted to quantitative microstructural characteristics including, average grain size and average fraction of LAGBs. These microstructural characteristics offer direct means to predict an array of performance attributes because (a) average grain size from SPD essentially controls the flow strength of the resulting material via the usual Hall-Petch relationship and (b) GB characteristics encapsulated by the LAGB fraction can be used to determine properties like effective diffusion, mobility and grain growth behaviors. The map can also be used to determine whether the resulting microstructure will be unimodal or multimodal and potentially estimate the ductility of the component. RSM map also delineates region where recrystallization will occur and hence conditions to produce coarse grained, low strength microstructure albeit thermally stable, and hence can be employed for high temperature applications. Together, the overarching vision of the development of such maps envisages a process design tool for creating customizable fine-grained materials and surfaces using SPD processes such as orthogonal machining to enable the design of novel multifunctional materials and products.

## Acknowledgments

This study was supported in part by the National Science Foundation (0826010, 0856626, 0927410) and the Nuclear Regulatory Commission (Faculty Development Grant). The authors would also like to thank the anonymous referees for their role in improving the manuscript and also suggesting future developments of the ideas proposed here.

## References

- [1] Cai, J., Shekhar, S., Wang, J., and Shankar, M. R., 2009, "Nanotwinned Microstructures From Low Stacking Fault Energy Brass by High-Rate Severe Plastic Deformation," *Scr. Mater.*, **60**(8), pp. 599–602.
- [2] Lee, S. G., Hwang, J. H., Shankar, M. R., Chandrasekar, S., and Compton, W. D., 2006, "Large Strain Deformation Field in Machining," *Metall. Mater. Trans. A*, **37**(5), pp. 1633–1643.
- [3] Swaminathan, S., Shankar, M. R., Lee, S., Hwang, J., King, A. H., Kezar, R. F., Rao, B. C., Brown, T. L., Chandrasekar, S., Compton, W. D., and Trumble, K. P., 2005, "Large Strain Deformation and Ultra-Fine Grained Materials by Machining," *Mater. Sci. Eng., A*, **410**, pp. 358–363.
- [4] Huang, C., Murthy, T. G., Shankar, M. R., M'saoubi, R., and Chandrasekar, S., 2008, "Temperature Rise in Severe Plastic Deformation of Titanium at Small Strain-Rates," *Scr. Mater.*, **58**(8), pp. 663–666.
- [5] Adibi-Sedeh, A. H., Madhavan, V., and Bahr, B., 2003, "Extension of Oxley's Analysis of Machining to Use Different Material Models," *Trans. ASME J. Manuf. Sci. Eng.*, **125**(4), pp. 656–666.
- [6] Calistes, R., Swaminathan, S., Murthy, T. G., Huang, C., Saldana, C., Shankar, M. R., and Chandrasekar, S., 2009, "Controlling Gradation of Surface Strains and Nanostructuring by Large-Strain Machining," *Scr. Mater.*, **60**(1), pp. 17–20.
- [7] Oxley, P. L. B., 1989, *The Mechanics of Machining: An Analytical Approach to Assessing Machinability*, Ellis Horwood Limited (A division of John Wiley & Sons), Chichester.
- [8] Shankar, M. R., Rao, B. C., Lee, S., Chandrasekar, S., King, A. H., and Compton, W. D., 2006, "Severe Plastic Deformation (SPD) of Titanium at near-Ambient Temperature," *Acta Mater.*, **54**(14), pp. 3691–3700.
- [9] Amouyal, Y., Divinski, S. V., Klinger, L., and Rabkin, E., 2008, "Grain Boundary Diffusion and Recrystallization in Ultrafine Grain Copper Produced by Equal Channel Angular Pressing," *Acta Mater.*, **56**(19), pp. 5500–5513.
- [10] Kawasaki, M., Horita, Z., and Langdon, T. G., 2009, "Microstructural Evolution in High Purity Aluminum Processed by ECAP," *Mater. Sci. Eng., A*, **524**(1–2), pp. 143–150.
- [11] Kuzel, R., Janacek, M., Matej, Z., Cizek, J., Dopita, M., and Srba, O., 2010, "Microstructure of Equal-Channel Angular Pressed Cu and Cu-Zr Samples Studied by Different Methods," *Metall. Mater. Trans. A*, **41**, pp. 1174–1190.
- [12] Shekhar, S., Cai, J., Lee, S., Wang, J., and Shankar, M. R., 2009, "How Strains and Strain-Rates Are Accommodated by Dislocations and Twins During Chip Formation by Machining," *Transactions of North American Manufacturing Research Institute/Society of Manufacturing Engineers (NAMRI/SME)*, **37**, pp. 637–644.
- [13] Gupta, R. K., Raman, R. K. S., and Koch, C. C., 2010, "Fabrication and Oxidation Resistance of Nanocrystalline Fe10Cr Alloy," *J. Mater. Sci.*, **45**(17), pp. 4884–4888.
- [14] Hoog, C. O., Birbilis, N., and Estrin, Y., 2008, "Corrosion of Pure Mg as a Function of Grain Size and Processing Route," *Adv. Eng. Mater.*, **10**(6), pp. 579–582.
- [15] Jeelani, S., and Scott, M. A., 1988, "How Surface Damage Removal Affects Fatigue Life," *Int. J. Fatigue*, **10**(4), pp. 257–260.
- [16] Misra, R. D. K., Thein-Han, W. W., Pesacreta, T. C., Hasenstein, K. H., Somani, M. C., and Karjalainen, L. P., 2009, "Favorable Modulation of Pre-Osteoblast Response to Nanogained/Ultrafine-Grained Structures in Austenitic Stainless Steel," *Adv. Mater.*, **21**(12), pp. 1280–1285.
- [17] Misra, R. D. K., Thein-Han, W. W., Pesacreta, T. C., Hasenstein, K. H., Somani, M. C., and Karjalainen, L. P., 2009, "Cellular Response of Preosteoblasts to Nanogained/Ultrafine-Grained Structures," *Acta Biomater.*, **5**(5), pp. 1455–1467.
- [18] Raman, R. K. S., and Gupta, R. K., 2009, "Oxidation Resistance of Nanocrystalline Vis-a-Vis Microcrystalline Fe-Cr Alloys," *Corros. Sci.*, **51**(2), pp. 316–321.
- [19] Roland, T., Retraint, D., Lu, K., and Lu, J., 2006, "Fatigue Life Improvement Through Surface Nanostructuring of Stainless Steel by Means of Surface Mechanical Attrition Treatment," *Scr. Mater.*, **54**(11), pp. 1949–1954.
- [20] Saldana, C., Swaminathan, S., Brown, T. L., Moscoso, W., Mann, J. B., Compton, W. D., and Chandrasekar, S., 2010, "Unusual Applications of Machining: Controlled Nanostructuring of Materials and Surfaces," *Trans. ASME J. Manuf. Sci. Eng.*, **132**(3), 030908.
- [21] Tao, N. R., Tong, W. P., Wang, Z. B., Wang, W., Sui, M. L., Lu, J., and Lu, K., 2003, "Mechanical and Wear Properties of Nanostructured Surface Layer in Iron Induced by Surface Mechanical Attrition Treatment," *J. Mater. Sci. Technol.*, **19**(6), pp. 563–566.
- [22] Baretzky, B., Baro, M. D., Grabovetskaya, G. P., Gubicza, J., Ivanov, M. B., Kolobov, Y. R., Langdon, T. G., Lendvai, J., Lipnitskii, A. G., Mazilkin, A. A., Nazarov, A. A., Nogues, J., Ovidko, I. A., Protasova, S. G., Raab, G. I., Revesz, A., Skiba, N. V., Sort, J., Starink, M. J., Straumal, B. B., Surinach, S., Ungar, T., and Zhilyaev, A. P., 2005, "Fundamentals of Interface Phenomena in Advanced Bulk Nanoscale Materials," *Rev. Adv. Mater. Sci.*, **9**(1), pp. 45–108.
- [23] Hoffer, H. J., Averback, R. S., Hahn, H., and Gleiter, H., 1993, "Diffusion of Bismuth and Gold in Nanocrystalline Copper," *J. Appl. Phys.*, **74**(6), pp. 3832–3839.
- [24] Childs, T. H. C., Maekawa, K., Obikawa, T., and Yamanae, Y., 2000, *Metal Machining: Theory and Application*, Arnold Publishers, London.
- [25] Velasquez, J. D. P., Tidu, A., Bolle, B., Chevrier, P., and Fundenberger, J. J., 2010, "Sub-Surface and Surface Analysis of High Speed Machined Ti-6Al-4V Alloy," *Mater. Sci. Eng., A*, **527**(10–11), pp. 2572–2578.
- [26] Brown, T. L., Saldana, C., Murthy, T. G., Mann, J. B., Guo, Y., Allard, L. F., King, A. H., Compton, W. D., Trumble, K. P., and Chandrasekar, S., 2009, "A Study of the Interactive Effects of Strain, Strain Rate and Temperature in Severe Plastic Deformation of Copper," *Acta Mater.*, **57**(18), pp. 5491–5500.
- [27] Zener, C., and Hollomon, J. H., 1944, "Effect of Strain Rate Upon Plastic Flow of Steel," *J. Appl. Phys.*, **15**, pp. 22–33.
- [28] Nes, E., Marthinsen, K., and Brechet, Y., 2002, "On the Mechanisms of Dynamic Recovery," *Scr. Mater.*, **47**(9), pp. 607–611.
- [29] Nes, E., Pettersen, T., and Marthinsen, K., 2000, "On the Mechanisms of Work Hardening and Flow-Stress Saturation," *Scr. Mater.*, **43**(1), pp. 55–62.
- [30] Swaminathan, S., Shankar, M. R., Rao, B. C., Compton, W. D., Chandrasekar, S., King, A. H., and Trumble, K. P., 2007, "Severe Plastic Deformation (SPD) and Nanostructured Materials by Machining," *J. Mater. Sci.*, **42**(5), pp. 1529–1541.
- [31] Humphreys, F. J., and Hatherly, M., 2004, *Recrystallization and Related Annealing Phenomena*, Elsevier, New York.
- [32] Jata, K. V., and Semiatin, S. L., 2000, "Continuous Dynamic Recrystallization During Friction Stir Welding of High Strength Aluminum Alloys," *Scr. Mater.*, **43**(8), pp. 743–749.
- [33] Buffa, G., Hua, J., Shivpuri, R., and Fratini, L., 2006, "Design of the Friction Stir Welding Tool Using the Continuum Based Fem Model," *Mater. Sci. Eng., A*, **419**(1–2), pp. 381–388.
- [34] Bingert, J. F., 2003, "Transverse Texture and Microstructure Gradients in Friction-Stir Welded 2519 Aluminum," *Proceedings of 4th International Symposium on Friction Stir Welding*, Park City, UT.

- [35] Gottstein, G., Zabardjadj, D., and Mecking, H., 1979, "Dynamic Recrystallization in Tension-Deformed Copper Single Crystals," *Metal Sci.*, **13**(3–4), pp. 223–227.
- [36] Montheillet, F., and Le Coze, J., 2002, "Influence of Purity on the Dynamic Recrystallization of Metals and Alloys," *Phys. Status Solidi A*, **189**(1), pp. 51–58.
- [37] Xiao, G. H., Tao, N. R., and Lu, K., 2008, "Effects of Strain, Strain Rate and Temperature on Deformation Twinning in a Cu-Zn Alloy," *Scr. Mater.*, **59**(9), pp. 975–978.
- [38] Mishra, A., Kad, B. K., Gregori, F., and Meyers, M. A., 2007, "Microstructural Evolution in Copper Subjected to Severe Plastic Deformation: Experiments and Analysis," *Acta Mater.*, **55**(1), pp. 13–28.
- [39] Oxley, P. L. B., and Hasting, W. F., 1977, "Predicting the Strain Rate in the Zone of Intense Shear in Which the Chip Is Formed in Machining From the Dynamic Flow Stress Properties of the Work Material and the Cutting Conditions," *Proc. R. Soc. London, Ser. A*, **356**(1686), pp. 395–410.
- [40] Johnson, G. R., and Cook, W. H., 1983, *A Constitutive Model and Data for Metals Subjected to Large Strains, High Strain Rates and High Temperatures*, The Hague, The Netherlands, pp. 541–547.
- [41] White, G. K., and Collocott, S. J., 1984, "Heat Capacity of Reference Materials: Cu and W," *J. Phys. Chem. Ref. Data*, **13**(4), pp. 1251–1258.
- [42] Weiner, J. H., 1955, "Shear Plane Temperature Distribution in Orthogonal Cutting," *Trans. ASME*, **77**(8), pp. 1331–1338.
- [43] Andrade, U., Meyers, M. A., Vecchio, K. S., and Chokshi, A. H., 1994, "Dynamic Recrystallization in High-Strain, High-Strain-Rate Plastic-Deformation of Copper," *Acta Metall. Mater.*, **42**(9), pp. 3183–3195.
- [44] Wang, Y. M., Chen, M. W., Zhou, F. H., and Ma, E., 2002, "High Tensile Ductility in a Nanostructured Metal," *Nature*, **419**(6910), pp. 912–915.
- [45] Shekhar, S., Cai, J., Wang, J., and Shankar, M. R., 2009, "Multimodal Ultrafine Grain Size Distributions From Severe Plastic Deformation at High Strain Rates," *Mater. Sci. Eng., A*, **527**(1–2), pp. 187–191.
- [46] Zhao, Y. H., Topping, T., Bingert, J. F., Thornton, J. J., Dangelewicz, A. M., Li, Y., Liu, W., Zhu, Y. T., Zhou, Y. Z., and Lavernia, E. L., 2008, "High Tensile Ductility and Strength in Bulk Nanostructured Nickel," *Adv. Mater.*, **20**(16), pp. 3028–3033.
- [47] Valiev, R. Z., Alexandrov, I. V., Zhu, Y. T., and Lowe, T. C., 2002, "Paradox of Strength and Ductility in Metals Processed by Severe Plastic Deformation," *J. Mater. Res.*, **17**(1), pp. 5–8.
- [48] Witkin, D., Lee, Z., Rodriguez, R., Nutt, S., and Lavernia, E., 2003, "Al-Mg Alloy Engineered With Bimodal Grain Size for High Strength and Increased Ductility," *Scr. Mater.*, **49**(4), pp. 297–302.
- [49] Han, B. Q., Lee, Z., Witkin, D., Nutt, S., and Lavernia, E. J., 2005, "Deformation Behavior of Bimodal Nanostructured 5083 Al Alloys," *Mater. Trans. A*, **36**(4), pp. 957–965.
- [50] Seviliano, J. G., and Aldazabal, J., 2004, "Ductilization of Nanocrystalline Materials for Structural Applications," *Scr. Mater.*, **51**(8), pp. 795–800.
- [51] Zhao, Y. H., Bingert, J. E., Liao, X. Z., Cui, B. Z., Han, K., Sergueeva, A. V., Mukherjee, A. K., Valiev, R. Z., Langdon, T. G., and Zhu, Y. T. T., 2006, "Simultaneously Increasing the Ductility and Strength of Ultra-Fine-Grained Pure Copper," *Adv. Mater.*, **18**(22), pp. 2949–2953.
- [52] Bokstein, B., Ivanov, V., Oreshina, O., Peteline, A., and Peteline, S., 2001, "Direct Experimental Observation of Accelerated Zn Diffusion Along Triple Junctions in Al," *Mater. Sci. Eng., A*, **302**(1), pp. 151–153.
- [53] Shekhar, S., and King, A. H., 2008, "Strain Fields and Energies of Grain Boundary Triple Junctions," *Acta Mater.*, **56**(19), pp. 5728–5736.
- [54] Shvindlerman, L. S., and Gottstein, G., 2001, "Grain Boundary and Triple Junction Migration," *Mater. Sci. Eng., A*, **302**(1), pp. 141–150.
- [55] Huang, Y., and Humphreys, F. J., 1999, "Measurements of Grain Boundary Mobility During Recrystallization of a Single-Phase Aluminium Alloy," *Acta Mater.*, **47**(7), pp. 2259–2268.
- [56] Gottstein, G., King, A. H., and Shvindlerman, L. S., 2000, "The Effect of Triple-Junction Drag on Grain Growth," *Acta Mater.*, **48**(2), pp. 397–403.